Ignition Desensitization of PBX *via* Aluminization

SEOKPUM KIM, YASUYUKI HORIE, and MIN ZHOU

The ignition behavior of aluminized HMX/Estane PBX under impact loading is analyzed through meso-scale simulations which account for constituent elasticity, viscoelasticity, elasto-viscoplasticity, fracture, internal contact, frictional heating, and heat conduction. The analyses involve explicit tracking of hotspot development and focuses on the probability of ignition, accounting for stochastic variations in microstructures which have HMX grain sizes ranging from 50 to 400 μm, binder-grain bonding strength of 35 MPa, and binder-grain interface bonding energy on the order of 81 J/m^2. For the microstructure configuration studied, it is found that aluminization with particles 50 μm in diameter delays the initiation of chemical reaction in the material. The mean time to ignition (t_{50}) for cases with 6 to 18 pct Al by volume is 1 to 1.7 μs longer (24 to 60 pct delay) as compared to that for the corresponding unaluminized PBX. To understand the mechanisms leading to the ignition delay, the differences in overall internal stresses, dissipations due to fracture and inelasticity, and hotspot field characteristics are quantified.

I. INTRODUCTION

SOME modern high explosive mixtures contain aluminum particles for enhanced performance.[1] Historically, the initial purpose of using Al, at least for some explosive formulators, was to improve the mixing of explosive crystals in binders,[2] as it is known that the inclusion of aluminum decreases the viscosity of PBX.[3,4] Studies have been conducted on not only the mechanism through which Al particles affect the performance, but also on desired timing for the addition of the particles and how they affect the microstructure of the materials. However, there has been little basic scientific research on the influence of aluminum addition on explosive ignition and ignition sensitivity, be it in the context of accidental insults or design loads. A few exceptions to this statement are the papers that have reported a desensitizing effect of Al particle addition in drop weight test.[4,5]

In this paper, we report a first attempt to analyze this issue computationally by focusing on one configuration of a HMX/Estane PBX. The approach we use is based on a cohesive finite element method (CFEM) we developed in the last few years for PBXs and granular explosives.[6–10] This framework accounts for finite elasticity, viscoelasticity, viscoplasticity, internal fracture, contact, friction, frictional heating, and heat conduction. The overall analyses also entail the use of a hotspot-based ignition criterion and a scheme to quantify the size-temperature states of hotspots in the

overall microstructures and in the energetic phase of the microstructures more specifically.[8] The extension here in this paper beyond the previous studies is to add Al to the constituents considered. The calculations quantify the response of the PBX and identify trends which can be used for future, more systematic studies on the behavior of aluminized PBXs. In particular, the calculations presented in this paper are limited to the addition of one population of mono-sized Al particles. The microstructures are designed in a way to keep the total solid (Al and HMX) fraction constant, while the fraction of the HMX is adjusted accordingly as the Al fraction is increased. We adopted this methodology following the practice in the publically available literature on the effect of Al addition.[4,5,11–13] The goal here is to identify a possible desensitizing effect of Al in low velocity impact loading that is beyond the effect of reduced fractions of solid explosive crystals in an overall PBX. As will become clear, the trend identified by numerical simulations is in qualitative agreement with available experimental data in the literature.

II. FRAMEWORK OF ANALYSIS

A. *Materials*

The microstructures considered are those of a PBX system consisting of either two (HMX/Estane) or three (HMX/Estane/Al) phases. The HMX grains have multi-faceted edges and a bimodal grain size distribution. The average grain sizes of the large and small grains are 289 and 123 μm, respectively. The microstructures generated for the two-phase PBX system is compared to a digitized micrograph of PBX 9501 using the two-point correlation function. Good agreement is found between the function profiles for the computationally generated microstructure and the actual microstructure.[14] Details

SEOKPUM KIM, Graduate Student, and MIN ZHOU, Professor, are with The George W. Woodruff School of Mechanical Engineering, Georgia Institute of Technology, Atlanta, GA 30318. Contact e-mail: min.zhou@gatech.edu YASUYUKI HORIE is recently retired from Munitions Directorate, Air Force Research Lab, Eglin AFB, FL 32542.

of the microstructural attributes of the two-phase (HMX/binder) PBX and the method used to generate the microstructure are described in Reference 14. To generate the three-phase system of microstructures, aluminum particles are added to the solid phase of the two-phase (HMX/binder) system. The volume fraction of the Al particles is varied from 0 to 18 pct. Accordingly, the volume fracture of the HMX grains is varied from 81 to 63 pct. While the volume fractions of the individual constituents are different in the different samples, the total volume fraction of solid load (HMX and Al) remains constant at 81 pct. Consequently, the volume fraction of the Estane binder is 19 pct for all samples. The volume fraction range of Al considered corresponds to an Al mass fraction of 0 to 25 pct, which is the range of interest for aluminized PBX in experiments.[1,15,16] The aluminum particles in the three-phase PBX microstructures have circular shapes and an average size of 50 μm. Typical Al particles in PBXs used in experiments have sizes that varies from sub-microns to 150 microns,[1,16] spherical or flake shapes, and monomodal size distributions.[17] Figure 1 shows the five microstructure conditions (with the different volume fractions of HMX grains and Al particles) studied. These images present one sample for each of the five microstructure conditions. Twenty random instantiations or microstructure samples are generated for each of the five cases in Figure 1. The 20 samples for each condition have the same statistical attributes (inducing grain size distribution, average grain size, and the same two-point correlation function profile, and *etc.*) and the same constituent volume fractions. Ten samples among the twenty instantiations with 10 pct Al contents are shown in Figure 2. Samples between different sets have the same attributes of HMX grains. Figure 3 shows the size distribution of HMX grains for each of the five cases in Figure 1. The size distribution profile of HMX from one set resembles that from another set. More details on the statistical similarity

between samples in a microstructure set can be found in References 9, 14.

In the analyses carried out here, the behavior of HMX granules follows a hyperelastic constitutive model and admits cohesive fracture above its fracture limit. In the loading regime of interest (non-shock low velocity impact), the HMX crystals are often assumed to undergo very little plastic deformation, since HMX is known to be brittle at the ambient pressure.[18] The Estane binder follows a generalized Maxwell viscoelastic model. Details of the constitutive models for the HMX grains and the binder are described in Reference 10.

The behavior of Al follows an elastic-viscoplastic model. The specific form of the constitutive relations used is

$$\hat{\tau} = \mathbf{L} : (\mathbf{D} - \mathbf{D}_p), \qquad [1]$$

where $\mathbf{L}$ is the tensor of elastic moduli. For isotropic elastic response,

$$\mathbf{L} = \frac{E}{1 + v}\left(\mathbf{I}' + \frac{v}{1 - 2v}\mathbf{I} \otimes \mathbf{I}\right). \qquad [2]$$

Here, $\mathbf{I}'$ is the fourth order identity tensor, E is Young's modulus, v is Poisson's ratio, α is the thermal expansion coefficient. $\mathbf{D}$ in Eq. [1] is the rate of defor-

Fig. 1—Microstructures with different Al volume fractions ($\eta_{Al} = 0$ to 0.18) and HMX volume fractions ($\eta_{HMX} = 0.81$ to 0.63). Each image shown represents one sample in a set of twenty statistically similar samples which are random instantiations of the same microstructure condition. Ten of the 20 instantiations for the set with 10 pct Al are shown in Fig. 2.
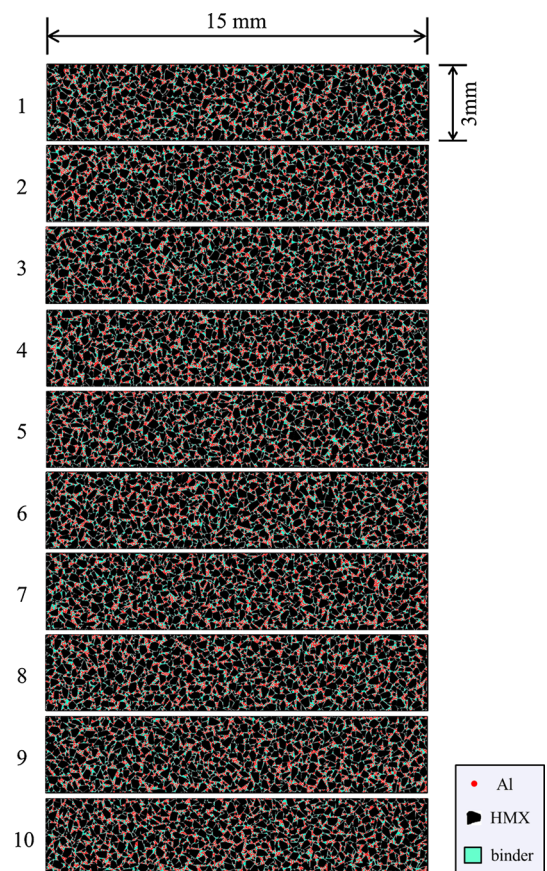
Fig. 2—Multiple samples of computationally generated, statistically similar microstructures with a volume fraction of 71 pct for HMX and 10 pct for Al.
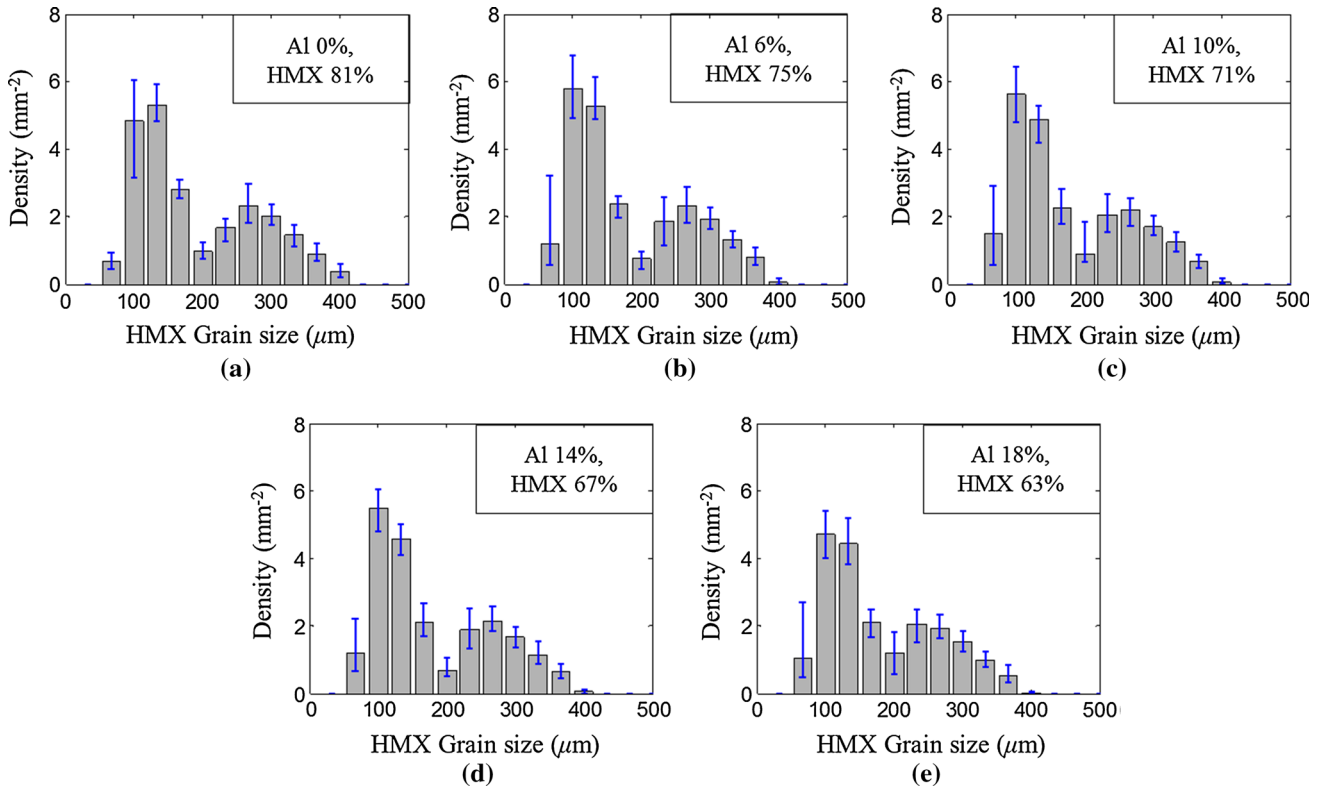
Fig. 3—Size distributions of HMX grains for each of the microstructure sets are shown in Fig. 1. The error bars illustrate the density range among the 20 samples in each set.

mation, which can be decomposed into elastic part and viscoplastic part as

$$\mathbf{D} = \mathbf{D}_e + \mathbf{D}_p, \quad [3]$$

where $\mathbf{D}_p$ is the viscoplastic part of $\mathbf{D}$ in the form of

$$\mathbf{D}_p = \frac{3\dot{\bar{\varepsilon}}}{2\bar{\sigma}}\tau', \quad \text{with } \bar{\sigma}^2 = \frac{3}{2}\tau' : \tau'. \quad [4]$$

Here, $\bar{\sigma}$ is the Misses equivalent stress, τ' is the deviatoric part of the Kirchhoff stress which is the product of the Jacobian and the Cauchy stress, and $\dot{\bar{\varepsilon}}$ is the equivalent plastic strain rate which has the form of

$$\left. \begin{array}{l} \dot{\bar{\varepsilon}} = \dfrac{\dot{\bar{\varepsilon}}_1 \dot{\bar{\varepsilon}}_2}{\dot{\bar{\varepsilon}}_1 + \dot{\bar{\varepsilon}}_2}, \\[2mm] \dot{\bar{\varepsilon}}_1 = \dot{\bar{\varepsilon}}_0 \left[\dfrac{\bar{\sigma}}{g(\bar{\varepsilon}, \mathrm{T})} \right]^{\mathrm{n}}, \\[2mm] \dot{\bar{\varepsilon}}_2 = \dot{\bar{\varepsilon}}_{\mathrm{m}} \exp[-a\, g(\bar{\varepsilon}, \mathrm{T})], \\[2mm] g(\bar{\varepsilon}, \mathrm{T}) = \sigma_0 \left(1 + \dfrac{\bar{\varepsilon}}{\varepsilon_0} \right)^N \left\{ 1 - \beta \left[\left(\dfrac{\mathrm{T}}{\mathrm{T}_0} \right)^{\kappa} - 1 \right] \right\}. \end{array} \right\} \quad [5]$$

The above relations consider strain hardening, strain rate dependence of plasticity, and thermal softening. More details of the above constitutive relations and descriptions of the parameters can be found in Reference 19. Values of the parameters for Al used here are listed in Table I. These parameters are chosen to describe the stress–strain behavior 7570 Al alloy[20] over

Table I.   Material Parameters Used for Aluminum

Parameters		Values (Unit)
Young's Modulus E		70 (GPa)
Poisson's Ratio v		0.33
Density ρ		2.80 (g/cm^3)
Parameters in Eq. [5]	n	50.0
	a	5.0
	$\dot{\bar{\varepsilon}}_0$	1.0×10^{-4} (s^{-1})
	$\dot{\bar{\varepsilon}}_{\mathrm{m}}$	8.0×10^{8} (s^{-1})
	σ_0	415 (MPa)
	ε_0	6×10^{-3}
	N	0.07
	β	0.035
	κ	3

the strain rate range of $1 - 10^6$/s. Figure 4 shows a comparison of the stress–strain behavior in Reference 20 the behavior described by the model utilized in this analysis. Again, just like the microstructure morphologies and other constitutive and interfacial parameters, the parameters for Al used here represent just one specific material data set. More systematic parametric studies can and should be carried out in the future.

B. Loading Configuration

The microstructures are initially stress-free and at rest. The sample size is 15 mm × 3 mm. Impact loading
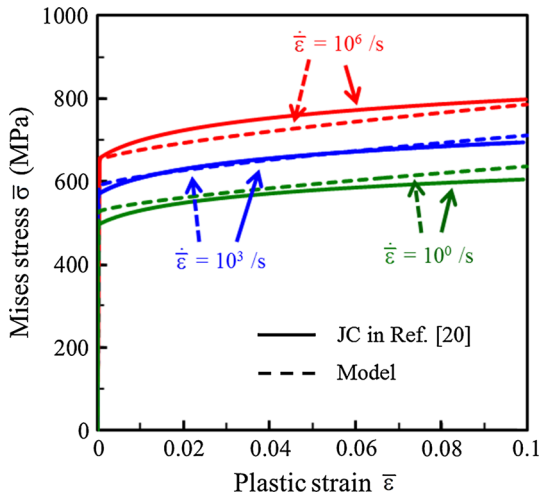
Fig. 4—Comparison of viscoplastic stress–strain profiles for Al from the Johnson–Cook model in Ref. [20] (indicated in solid line) and the viscoplastic model based on Ref. [19] with parameters in Table I (indicated in dotted line).
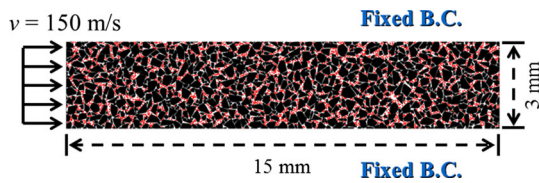
Fig. 5—Configuration of loading and boundary conditions considered.

is affected by applying a boundary velocity at the left end of the samples, as shown in Figure 5. A linear velocity ramp is specified over the initial 0.5 μs of loading ($0 \leq t \leq 0.5 \mu$s). Specifically, the boundary velocity is linearly increased from zero to the maximum of $v = 150$ m/s over this period. The top and bottom side boundaries are constrained such that vertical motions do not occur. This configuration approximates the normal impact loading of an infinitely wide material block under the conditions of macroscopically uniaxial strain. For all calculations presented, initial temperature is $T = 300$ K.

C. Cohesive Finite Element Framework

The analysis utilizes a Lagrangian cohesive finite element method (CFEM) framework which allows finite deformation, thermo-mechanical coupling, failure in the form of cracks, and frictional heating to be tracked and analyzed. The details of CFEM are described in Barua et al.[10] The framework includes cohesive elements having initially zero thickness embedded along all element boundaries throughout the microstructure to track arbitrary crack path and fracture patterns. A schematic representation of the bi-linear traction-separation law that determines the behavior of the cohesive crack faces is shown in Figure 6. The area underneath the traction-separation graph represents the bonding energy or fracture energy of the interface.
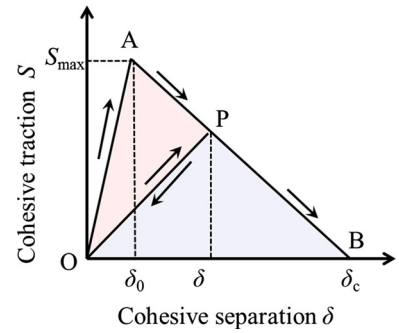
Fig. 6—Bilinear traction-separation law for potential cracks.

Table II. Cohesive Parameters for the Al/Polymer Interface

Parameters	Values (Unit)
δ_c	4.71 (μm)
δ_0	0.236 (μm)
S_{max}	70 (MPa)

The interfacial bonding energy between Al and polymers varies, according to experiments.[21-23] The cohesive parameters for the interface between the Al particles and the polymer binder have been chosen based on a bonding energy of 165 J/m^2 reported from UDCB tests in Reference 23. These interface cohesive parameters are listed in Table II. The cohesive parameters for HMX, Estane, and the HMX-Estane interfaces have previously been reported in Reference 10.

D. Ignition Criterion

A recently developed criterion for ignition[8] is used to determine the onset of irreversible chemical decomposition of the HMX phase in the PBX samples. This criterion provides a relationship between the size and the temperature states of critical hotspots. Specifically,

$$d(T) \geq d_c(T), \qquad [6]$$

where d is the diameter of a hotspot resulting from a loading event whose interior temperatures are at or above temperature T and d_c is the minimal diameter of a hotspot required for thermal runaway at temperature T. The quantitative information regarding the right-hand side of Eq. [6] is taken from the work of Tarver et al.[24] who performed chemical kinetics calculations to analyze the criticality issue for HMX and TATB explosives. The calculations consider multistep reaction mechanisms and the pressure and temperature dependence of reactants and products. More details about the ignition criterion can be found in Reference 8.

The left-hand side of Eq. [6] is obtained by analyzing the temperature fields in the microstructures from CFEM calculations. To account for the variations of temperature within a hotspot (note that temperatures at different spatial locations within a hotspot are different and the temperature threshold is the lowest temperature at the periphery), the hotspot threshold of Tarver et al. is treated as a band of ±10 pct about the

mean value, as in Reference 8. A hotspot is considered to be critical when it crosses the lower threshold limit (90 pct of the average value). Taking into consideration the stochastic nature of arbitrary microstructures, we employ an approach to identify the time to criticality t_c measured from the onset of loading. Specifically, instead of one single hotspot, criticality is regarded as being reached if the critical hotspot density in a specimen reaches a level equal to or greater than 0.22 mm^{-2}. This level corresponds to two critical hotspots in a 3 mm square domain.

Although the heat of reaction per unit mass of Al is higher than that of HMX, the reaction of Al is relatively slow and requires high activation energy because of an oxidation coating around the Al surface.[1] Therefore, aluminum acts as an inert material in the reaction zone of the detonation front.[25] The melting temperatures of Al and Al_2O_3 are 930 K and 2300 K (657 °C and 2027 °C), respectively, whereas a typical hotspot of HMX reaches criticality below 900 K (627 °C), according to the ignition criterion used and hotspot sizes we encounter in the HMX phase. Since the initiation of Al reaction is induced by the energy released from the decomposition of HMX, the initiation of HMX dominates the criticality of aluminized PBXs. For these reasons, the ignition criterion in Eq. [6] is applied only to the analysis of the temperature field in the HMX granules in the aluminized PBX microstructures.

E. Statistical Model

The analysis is performed in the following steps. First, calculations are carried out using the five sets of microstructure instantiations described in Section II–A, under the loading condition shown in Figure 5. Following the calculations, the ignition criterion described in Section II–D is used to scan the microstructures for hotspots and detect critical hotspots that have reached the size-temperature threshold. With this approach, once an ensemble (or a set of microstructure instantiations) is analyzed, the distribution of the time to criticality can be uniquely determined for the microstructure set. For each set with a given combination of statistically similar attributes, the time to criticality (t_c) is evaluated as a cumulative probability distribution. The distribution of the time to criticality obtained from each set is fitted to the Weibull distribution with three parameters[26] in the form of

$$P(t) = 1 - e^{-\Phi(t)}, \quad \Phi(t) = \begin{cases} 0, & t \leq t_0 \\ \left(\frac{t-t_0}{\tau}\right)^m, & t \geq t_0; \end{cases} \quad [7]$$

where t is the time to criticality, t_0 is the minimum time to criticality, or the cutoff time to criticality below which the probability of ignition is zero, τ is a time-scaling parameter that affects the slope of the distribution curve, and m is a shape parameter.

Barua et al.[9] provided a physical basis for the Weibull distribution interpretation of the probability of time to criticality using Terao's model.[27] They showed that $m = 2$ for loading conditions involving a propagating

stress wave front without reflection from boundaries of the a sample (the right-hand boundary for the configuration in Figure 5 and throughout this paper).

III. RESULTS AND DISCUSSION

A systematic numerical study is carried out, focusing on the effect of the volume fraction of aluminum on ignition. Parameters such as stress, crack length, and frictional dissipation are analyzed. The probability of ignition is obtained *via* fits to the Weibull distribution for each of the cases studied.

A. Stress Profiles

Aluminized PBX is known to have higher performance in terms of energy output (up to 25 pct in terms of power of explosion[1] or up to 30 pct in terms of work of explosion[25]), depending on measurement. However, the detonation pressure and detonation velocity of aluminized PBX are lower than those of unaluminized PBX,[28, 29] since aluminum particles do not react at the detonation front, and instead, generate a secondary blast at later stages. In contrast to the well-known effects of Al on the performance, there have been few studies on the effect of aluminum on stress in PBXs under non-shock loading. Chakravarthy et al.[30] analyzed the stress profiles in granular explosives and found no significant change in hydrostatic stress or von Mises stress resulting from the addition of aluminum particles in the low velocity regime ($v < 200$ m/s).

Our results show that there is no significant change in the plateau level of the longitudinal stress as the volume fraction of aluminum is increased from 6 to 18 pct. Figure 7 shows the spatial profiles of the average longitudinal stress at $t = 4$ μs. For the aluminized PBX, the stress front shows an elastic precursor, followed by a slower increase which is indicative of plasticity. This effect of plasticity becomes more pronounced as Al content increases. Specifically, the stress histories for cross-sections at $x = 2, 6, 10$ mm are plotted in Fig. 8 for the cases with 0 and 10 pct Al. The increasing difference between the stress profiles for the unaluminized
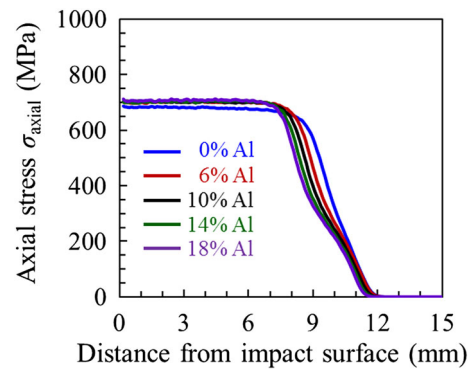
Fig. 7—Profiles of axial stress for unaluminized HMX/Estane PBX and aluminized PBX with Al contents between 6 and 18 vol pct at $t = 4$ μs.
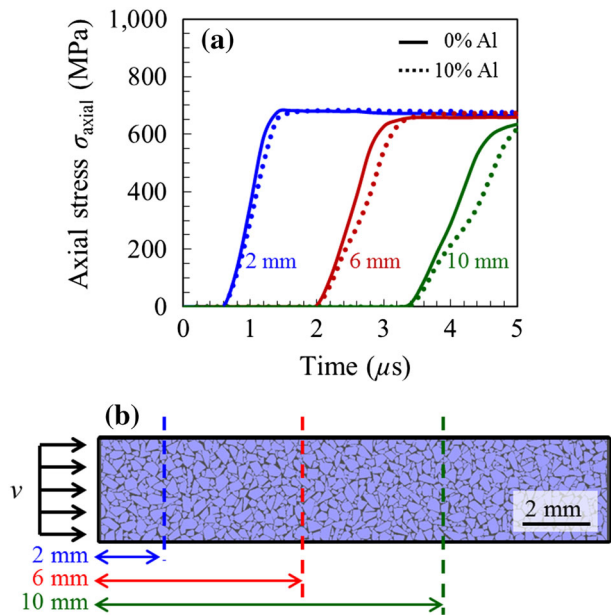
Fig. 8—History of axial stress for unaluminized HMX/Estane PBX (*solid line*) and aluminized PBX with 10 pct Al contents (*dotted line*) for the locations of $x = 2, 6, 10$ mm.
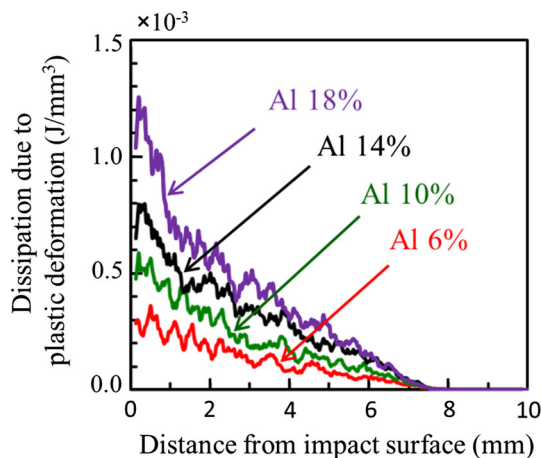
Fig. 9—Profiles of density of energy dissipation due to plastic deformation for microstructures with Al contents between 6 and 18 vol pct at $t = 4$ μs.

PBX and the aluminized PBX indicates that, as the stress wave propagates through the material, longer times are required for the aluminized PBX to reach a steady state of stress. The plasticity of Al and the sliding along Al-binder interfaces caused by the addition of the Al particles lead to an overall weakening of the composite material. This issue will be further analyzed in the future.

B. *Effect of Aluminum on Energy Dissipation*

Figure 9 shows a snapshot at $t = 4$ μs of the energy dissipation per unit volume of material resulting from plastic deformation for microstructures with 6 to 18 pct

aluminum by volume. As in Figure 7, the profiles show variation along the loading direction, between the wave front and the impact face. Since only aluminum is elastic-viscoplastic and, therefore, has dissipation due to plasticity, higher aluminum content leads to higher levels of plastic dissipation. Note that, for the time shown, plastic dissipation (and therefore plasticity by inference) begins to occur at a distance of approximately 7 mm from the impact face. This location roughly coincides with the peaking of the stress profiles in Figure 7. This synchrony supports the interpretation that the plasticity weakens the composite material and lowers the overall stress.

Figure 10(a) shows the effect of aluminum on the length density of all cracks (red) and the length density of cracks associated with the HMX grains only (cracks within HMX grains and interfacial cracks between HMX and binder, blue). As more aluminum is added to the materials, less number of HMX particles remain in the microstructure, because aluminum particles replace HMX granules (total solid volume fraction is constant). Therefore, crack density associated with the HMX grains decreases as the volume fraction of aluminum increases. Since the aluminum particles (50 μm in diameter) are smaller than the smaller group of HMX grains (123 μm average diameter), the total sum of surface area of aluminum and HMX granules increases as the aluminum content increases. For this reason, length density of all cracks increases as the volume fraction of aluminum increases.

Frictional dissipation in HMX grains is an important mechanism responsible for the development and evolution of hotspots,[7,31] and consequently has a profound impact on hotspot-induced ignition of PBXs. It is important to analyze the frictional dissipation at cracks associated with HMX grains. Figure 10(b) shows the frictional dissipation per unit crack length at cracks associated with the HMX phase. The profile indicates that frictional dissipation at cracks is relatively more intense for the unaluminized HMX/polymer PBX than for the aluminized PBXs. This difference directly affects the hotspot fields in these materials, as discussed below.

C. *Hotspot Quantities and Ignition Probability*

In this section, we analyze the hotspot area fraction (fraction of material within hotspots above a certain temperature threshold) and the hotspot number density (number of hotspots per unit volume of material). A threshold of $T = 400$ K is used as the threshold temperature for hotspot demarcation. The temperature fields for all microstructures at $t = 4$ μs after onset of loading are analyzed. At this time, the peak stress reaches a distance of approximately 7 mm from the impact face and fracture initiates in the granules. The fracture leads to frictional dissipation along crack faces. Locations closer to the loading face is subject to longer and more intense loading, as a result, experience more extensive failure, deformation and heating due to deformation and friction. Consequently, more significant heating is observed near the impact surface and ignition is in general a result of hotspots in this region.
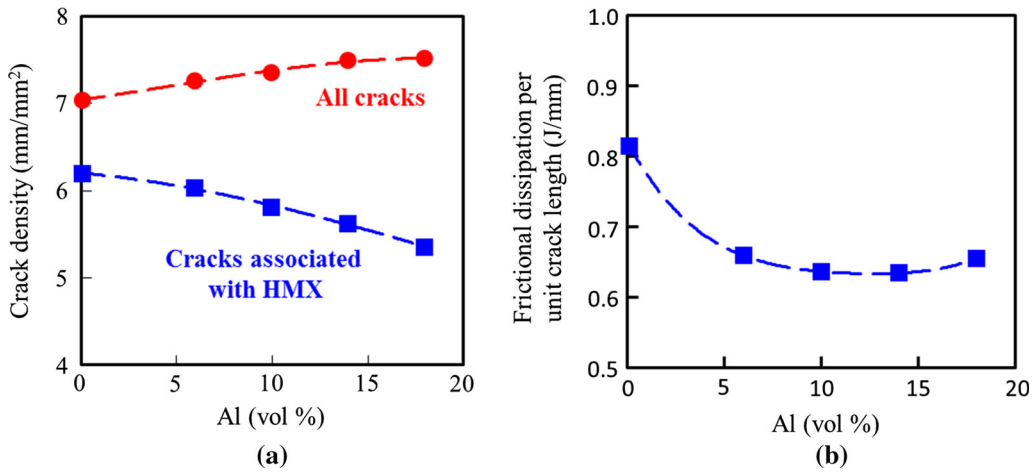
Fig. 10—Effect of Al addition on crack densities and frictional dissipation at $t = 4$ μs; (a) all crack density (red), and density of cracks associated with HMX (blue); (b) frictional dissipation per unit length of cracks associated with the HMX phase.
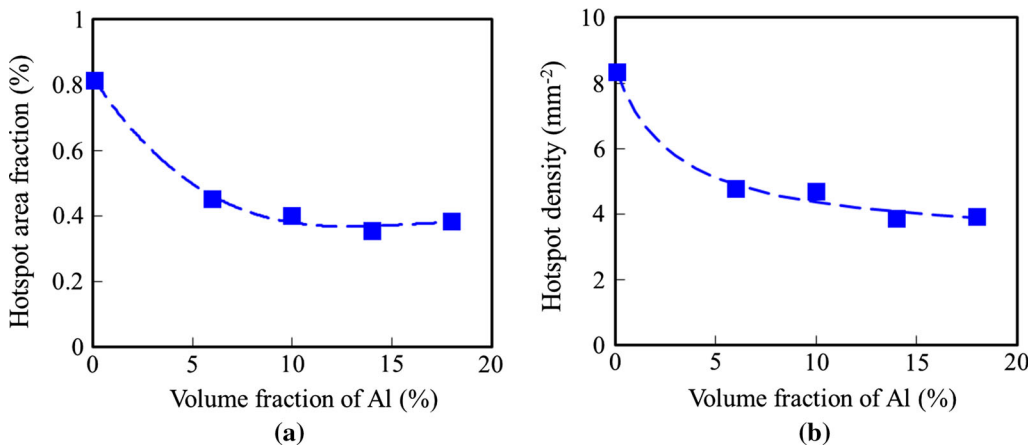
Fig. 11—Effect of Al addition on hotspot counts; (a) hotspot area fraction; (b) hotspot number density at $t = 4$ μs.

The hotspot counts reported here concern first 3 mm of the long samples, or more specifically, the top 3 mm × 3 mm portion of the samples. Figures 11(a) and (b) show hotspot area fraction and the average hotspot number density, respectively. The addition of aluminum particles significantly decreases the hotspot counts, indicating that the aluminized PBXs are less susceptible to creating hotspots that may result in ignition relative to the unaluminized PBX. Note that frictional dissipation per unit crack length (Figure 10(b)) shows a trend that is consistent with that of the hotspot counts (Figure 11). Also frictional dissipation per unit crack length does not change significantly with the aluminum content over the Al volume fraction range of 10 to 18 pct, although a significant difference is seen between that for the unalumnized PBX and that for the aluminized PBXs. A similar trend is seen in the hotspot fields as measured by the hotspot area fraction and hotspot density.

The ignition probability is shown in Figure 12 is obtained from the five microstructure sets, each of which having twenty samples. The Weibull parameters of each volume fraction of aluminum are listed in Table III. The

PBX without aluminum has relatively earlier ignition times than the aluminized PBXs. This may be interpreted to mean that adding aluminum in PBX makes the material less sensitive in terms of ignition time. In particular, adding Al causes the probability curves to flatten out to the right (longer times), such that the value of mean time to ignition (t_{50}) or the time by which 50 pct of the samples have reached criticality is higher for higher Al content. This finding is consistent with the experimental results by Prakash et al.[4] and Radwan[5] as they observed that the insensitivity (required height of impactor for explosion) of HMX based and RDX based PBX increases as Al content increases. However, the ignition probabilities of aluminized PBXs ($\eta_{Al} = 6$ to 18 pct) in Figure 12 lie close to each other and do not show a clear trend of change with Al volume fraction under the conditions analyzed here. Also, a few samples of the aluminized PBXs reach criticality earlier than the unaluminized PBX, indicating that aluminization may cause the "worst-case" ignition scenarios to become even "worse". Although the specific reason is unclear at this time, one possible explanation is that the morphological rearrangement of HMX caused by the addition
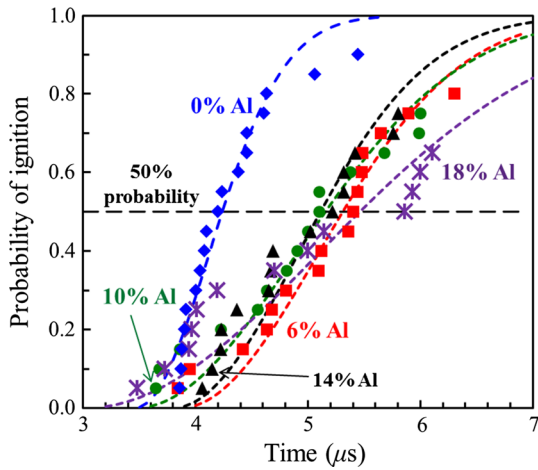
Fig. 12—Ignition probabilities for unaluminized PBX and aluminized PBX with 6 to 18 pct aluminum by volume.

Table III. Weibull Parameters for Data in Fig. 11

Al (Percent)	t_0 (μs)	τ (μs)
0	3.46	0.93
6	3.88	1.7
10	3.40	2.13
14	3.79	1.58
18	2.92	3.1

of Al may lead to closer contact of HMX grains in some samples, thereby, accelerating the development of hotspot in certain cases. More detailed analyses are needed to ascertain the reason and the trend over a wider range of Al content.

IV. CONCLUSIONS

The ignition behavior of PBX microstructures with 6 to 18 pct Al by volume is analyzed and compared to that of the corresponding unaluminized PBX. The mean time to ignition (t_{50}) for the aluminized PBXs delays by 1 to 1.7 μs (24 to 60 pct delay) as compared to that for the corresponding unaluminized PBX. To delineate the mechanisms responsible for the ignition delay, the differences in overall internal stress, dissipations due to fracture and inelasticity, and hotspot field characteristics are quantified. It is found that, for the material configuration studied, aluminization decreases the crack density and frictional energy dissipation in the HMX phase. Aluminization also causes the frictional dissipation per unit crack length to decrease. The lower dissipation may be partly due to the lower overall stress levels in the aluminized materials, which results from the relatively weak and somewhat compliant binder-Al interfaces considered here. Overall, the analyses present a preliminary study of the effect of aluminization of PBX for a particular material configuration. Specifically, the analyses consider only one level of interfacial

bonding between the binder and the Al particles. Also, only one Al particle size is considered. The fact that the stress front in the aluminized PBX is delayed relative to that in the unaluminized PBX suggests that plastic deformation and interfacial failure are extensive and significantly influence the behavior of the composites. It remains to be seen how the ignition behavior may change as other material configurations (with significantly different binder-Al interfacial bonding and Al particle sizes) are considered. This will be a topic for further studies.

REFERENCES

1. P.P. Vadhe, R.B. Pawar, R.K. Sinha, S.N. Asthana, and A.S. Rao: *Combust. Explos. Shock Waves*, 2008, vol. 44, pp. 461–77.
2. Y. Horie: in *Personal Communication with J. Leathy of Leathy Consulting*, J. Leathy of Leathy Consulting ed.
3. G. Antić and V. Džingalašević: *Sci. Tech. Rev.*, 2006, vol. 56, pp. 52–58.
4. V. Prakash, V.K. Phadke, R.K. Sinha, and H. Singh: *Def. Sci. J.*, 2004, vol. 54, pp. 475–82.
5. M. Radwan: in *32nd Int'l Annual Conference of ICT*, Karlsruhe, Germany, p. 44, 2001.
6. A. Barua, Y. Horie, and M. Zhou: *J. Appl. Phys.*, 2012, vol. 111, p. 054902.
7. A. Barua, Y. Horie, and M. Zhou: *Proc. R Soc. a-Math. Phys. Eng. Sci.*, 2012, vol. 468, pp. 3725–44.
8. A. Barua, S. Kim, Y. Horie, and M. Zhou: *J. Appl. Phys.*, 2013, vol. 113, p. 064906.
9. A. Barua, S. Kim, Y. Horie, and M. Zhou: *J. Appl. Phys.*, 2013, vol. 113, p. 184907.
10. A. Barua and M. Zhou: *Modell. Simul. Mater. Sci. Eng.*, 2011, vol. 19, p. 055001.
11. W.A. Trzcinski, S. Cudzilo, and L. Szymanczyk: *Propellants Explos. Pyrotech.*, 2007, vol. 32, pp. 392–400.
12. M.F. Gogulya, A.Y. Dolgoborodov, and M.A. Brazhnikov: *Chem. Phys. Rep.*, 1998, vol. 17, pp. 51–54.
13. A.S. Kumar, V.B. Rao, R.K. Sinha, and A.S. Rao: *Propellants Explos., Pyrotech.*, 2010, vol. 35, pp. 359–64.
14. S. Kim, A. Barua, Y. Horie, and M. Zhou: *J. Appl. Phys.*, 2014, vol. 115, p. 174902.
15. Y.L. Zhu, H. Huang, H. Ren, and Q.J. Jiao: *J. Energ. Mater.*, 2013, vol. 31, pp. 178–91.
16. A.M. Grishkin, L.V. Dubnov, V.Y. Davidov, Y.A. Levshina, and T.N. Mikhailova: *Combust. Explos. Shock Waves*, 1993, vol. 29, pp. 239–45.
17. C.G. Rumchik and J.L. Jordan: *AIP Conf. Proc.*, 2007, vol. 955, pp. 795–98.
18. D.J. Benson and P. Conley: *Modell. Simul. Mater. Sci. Eng.*, 1999, vol. 7, pp. 333–54.
19. M. Zhou, A. Needleman, and R.J. Clifton: *J. Mech. Phys. Solids*, 1994, vol. 42, pp. 423–58.
20. N.S. Brar, V.S. Joshi, and B.W. Harris: *Shock Compress. Condens. Matter, Pts 1 and 2,* 2009, vol. 1195, pp. 945–48.

21. J. Liu, M.K. Chaudhury, D.H. Berry, J.E. Seebergh, J.H. Osborne, and K.Y. Blohowiak: *J. Adhes. Sci. Technol.*, 2006, vol. 20, pp. 277–305.
22. J. Schultz, A. Carré, and C. Mazeau: *Int. J. Adhes. Adhes.*, 1984, vol. 4, pp. 163–68.
23. V. Sundararaman and S.K. Sitaraman: *J. Electron. Packag.*, 1999, vol. 121, pp. 275–81.
24. C.M. Tarver, S.K. Chidester, and A.L. Nichols: *J. Phys. Chem.*, 1996, vol. 100, pp. 5794–99.
25. T.L.J. John, F. Moxnes, and Erik. Unneberg: *Adv. Stud. Theor. Phys.*, 2013, vol. 7, pp. 1051–69.
26. Y. Li and M. Zhou: *J. Mech. Phys. Solids*, 2013, vol. 61, pp. 472–88.
27. K. Terao: *Irreversible Phenomena: Ignitions, Combustion and Detonation Waves* (Chap. 3), Springer, New York, 2007.
28. M.F. Gogulya, M.N. Makhov, A.Y. Dolgoborodov M.A. Brazhnikov, V.I. Arkhipov, and V.G. Shchetinin: *Combust. Explos. Shock Waves*, 2004, vol. 40, pp. 445–57.
29. L. Orth-Farrell and H. Krier: *Combust. Sci. Technol.*, 2000, vol. 161, pp. 69–88.
30. S. Chakravarthy, K.A. Gonthier, and R. Panchadhara: *Modell. Simul. Mater. Sci. Eng.*, 2013, vol. 21, p. 055016.
31. J.K. Dienes, Q.H. Zuo, and J.D. Kershner: *J. Mech. Phys. Solids*, 2006, vol. 54, pp. 1237–75.